



ELSEVIER

Contents lists available at ScienceDirect

## Mechanics of Materials

journal homepage: [www.elsevier.com/locate/mechmat](http://www.elsevier.com/locate/mechmat)

## Finite element simulation of the plastic collapse of closed-cell aluminum foams with X-ray computed tomography

Insu Jeon <sup>a,\*</sup>, Tadashi Asahina <sup>b</sup>, Ki-Ju Kang <sup>a</sup>, Seyoung Im <sup>c</sup>, Tian Jian Lu <sup>d</sup>

<sup>a</sup> School of Mechanical Systems Engineering, Chonnam National University, 300 Yongbong-dong, Buk-gu, Gwangju 500-757, Republic of Korea

<sup>b</sup> Materials Research Institute for Sustainable Development, National Institute of Advanced Industrial Science and Technology (AIST), Shimoshidami, Moriyama-ku, Nagoya 463-8560, Japan

<sup>c</sup> Department of Mechanical Engineering, Korea Advanced Institute of Science and Technology (KAIST), Daejeon 305-701, Republic of Korea

<sup>d</sup> MOE Key Laboratory for Strength and Vibration, School of Aerospace, Xi'an Jiaotong University, Xi'an 710049, PR China

### ARTICLE INFO

#### Article history:

Received 6 October 2008

Received in revised form 6 January 2010

#### Keywords:

Closed-cell Al foam

X-ray computed tomography

Finite element analysis

Plastic collapse

Energy absorption capacity

### ABSTRACT

The detailed deformation and plastic collapse mechanisms of closed-cell Al foams under uniaxial compressive loading, which govern the energy absorption capacity of the foam material, are analyzed with the method of finite elements and experimental measurements. A three-dimensional (3D) finite element (FE) model for a real closed-cell Al foam specimen fabricated via the direct foaming route is constructed by employing the micro-focus X-ray CT system, the 3D reconstruction program, the 3D scanned data processing software, and the commercially available mesh generation program. Finite element analysis is subsequently carried out using the constructed FE model to explore the deformation and collapse mechanisms of the foam specimen, and the numerical predictions are compared with the experimentally measured results. From this research, it is found that an increase in the 0.2% offset yield stress considerably increases the magnitude of the plateau stress, whereas a decrease in the power-law hardening exponent not only increases the magnitude of the plateau stress but also modifies the shape of the plateau stage. Also, it is found that an increase in the 0.2% offset yield stress with a decrease in the power-law hardening exponent dramatically increases the magnitude of the plateau stress.

© 2010 Elsevier Ltd. All rights reserved.

### 1. Introduction

Closed-cell metallic foams (e.g., aluminum or aluminum alloy foams) have been considered as a candidate material for designing lightweight energy absorbing components for automobiles, high speed trains and other transportation applications (Evans et al., 1999; Banhart, 2001). The energy absorption capacity of a typical Al foam having closed cells is characterized by a relatively long plateau stage on its compressive stress–strain curve. The magnitude of the stress at the beginning of the plateau stage, which is conveniently defined as plateau stress,  $\sigma_{pl}$ , is therefore a key parameter governing the energy absorption capacity of

the foam; another key parameter is the densification strain,  $\varepsilon_{df}$ , signifying the end of the plateau stage; see Fig. 1. As a good approximation, the product  $\sigma_{pl}\varepsilon_{df}$  can be taken as a quantitative measure of the energy absorbing capability of the foam. Therefore, the plateau stresses and deformation behaviors of Al foam materials with closed cells subjected to compressive load (both static and dynamic) have been actively investigated in the past decade (see, for example, amongst many others, Sugimura et al., 1997; Simone and Gibson, 1998; Andrews et al., 1999; Miyoshi et al., 1999).

A notable experimental analysis of the compressive deformation mechanisms in closed-cell Al foam was carried out using the techniques of X-ray computed tomography and surface strain mapping by Bastawros et al. (2000). They demonstrated that the plateau stage on the compressive

\* Corresponding author. Tel.: +82 62 530 1688; fax: +82 62 530 1689.  
E-mail address: [i\\_jeon@chonnam.ac.kr](mailto:i_jeon@chonnam.ac.kr) (I. Jeon).

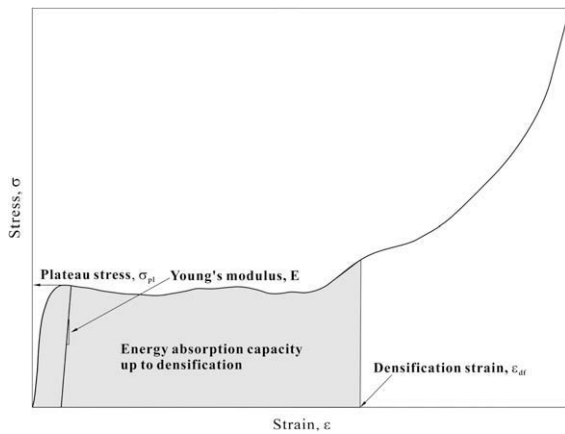


Fig. 1. Schematic compression curve of the closed-cell Al foam material.

stress versus strain curve of the foam is affected by discrete bands of strain localization that are formed and plastically collapsed in the foam material. In particular, they experimentally showed that the collapse of one of the bands results in the plateau stress.

Recently, Jeon and Asahina (2005) demonstrated that a small closed-cell Al foam specimen under compression is capable of exhibiting the stress–strain behavior identical to that of the bulk foam material, if the structural defects such as partially coupled cells, missing cells and collapsed cells are excluded (see Fig. 2). As a result, it is possible to numerically analyze the small closed-cell Al foam without any structural defects using the direct modeling process and the method of finite elements (Spanne et al., 1994; Brydon et al., 2005; Youssef et al., 2005; Toda et al., 2006) to investigate the deformation and failure mechanisms of the bulk foam material.

With the focus placed on increasing the energy absorption capacity of aluminum foams having closed cells, we

analyze in this research the detailed plastic collapse mechanisms of the foam subjected to static uniaxial compressive loading by 3D finite element (FE) modeling with X-ray computed tomography. Experimental measurements are carried out to validate the FE predicted foam compressive behavior. The effects of cell wall material properties, such as the 0.2% offset yield stress and power-law hardening exponent, on the compressive performance of the foam material are clarified. Based on the FE results and experimental measurements, an effective and efficient method for improving the energy absorption capacity of the foam material is suggested.

## 2. Finite element modeling of the foam material

Built upon the experimental results of Jeon and Asahina (2005), a relatively small 10 mm × 10 mm × 10 mm specimen of closed-cell Al foam ALPORAS® of Shinko Wire Co. Ltd., which was fabricated with the direct foaming method, was prepared for geometric modeling (see Fig. 3(a)). To prepare this specimen, several 10 mm × 10 mm × 10 mm foam samples were fabricated using the electrical discharge machine to ensure both the surface flatness and cleanliness for detecting structural defects in the specimens. Then, a specimen without any visible structural defect was carefully selected by means of surface observation with the digital microscopic system, VHX-100 of KEYENCE Corp. The average cell size was  $\bar{d} = 4.36$  mm and the relative density of the specimen was  $\rho/\rho_s = 0.0859$ . Here,  $\rho$  is the density of the Al foam, and  $\rho_s = 2.7$  g/Cm<sup>3</sup> is the density of the cell wall material.

The microfocus X-ray CT system of Shimadzu Corp. was used to scan the external and internal structures of the selected foam specimen. The scanned grayscale tomographic images are shown in Fig. 3(b). With these images, the foam specimen was reconstructed using 3D reconstruction program TRI/3D-BON of Ratoc System Engineering Co. Ltd. The profile of the solid cellular skeleton (continuous) and

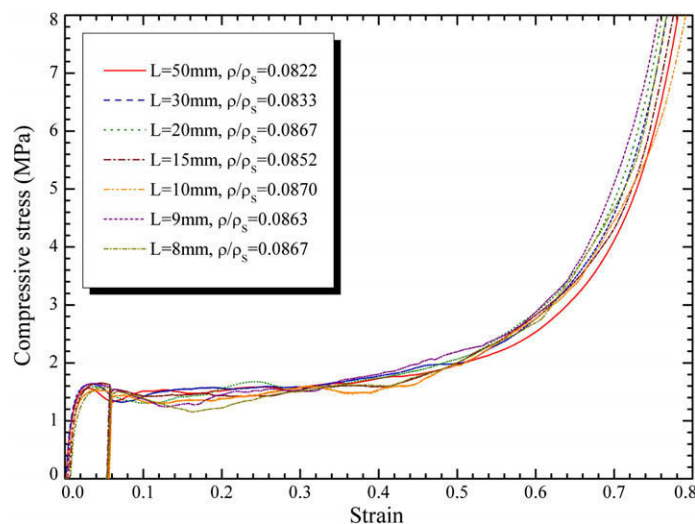
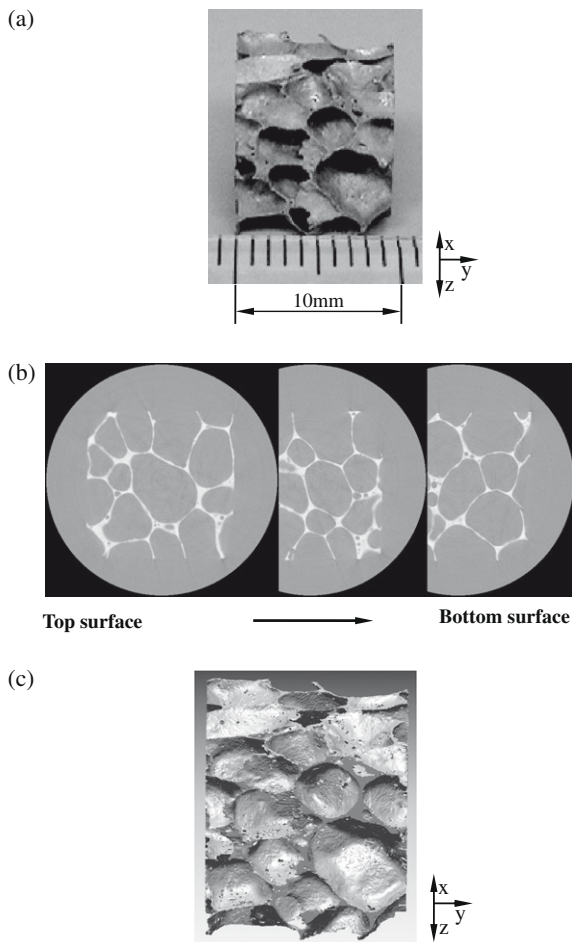


Fig. 2. Stress–strain curves of various size specimens without structural defects (Jeon and Asahina, 2005). Here,  $L$  is the edge length of a cube foam specimen,  $\rho$  is the density of the foam material, and  $\rho_s = 2.7$  g/Cm<sup>3</sup> is the density of the Al cell wall.



**Fig. 3.** (a) A 10 mm × 10 mm × 10 mm specimen without structural defects, (b) its tomographic images and (c) reconstructed model.

the air domain (discontinuous) in the tomographic images were binarized using this program, and the isolated small particles from the cellular skeleton in the binarized images were removed. The 3D cellular structure was then reconstructed using the marching cubes algorithm (see Fig. 3(c)) (Sone et al., 2004).

For 3D geometric modeling of the closed-cell foam specimen having an extremely complex structure, a completely new modeling procedure was applied. Fig. 4(a)–(f) provide an overview of the procedure for the creation of a geometric solid model through a Boolean operation using a nonuniform rationale B-spline (NURBS) surface fabricated from a separated and smoothed cell in the reconstructed model. The 3D scanned data processing software RapidForm™ of INUS Tech. Inc. was used to accomplish the above task (Shin et al., 2007). The cube-shaped frames in Fig. 4(a)–(c) represent the disjointed and separated status of a cell, while the bold solid lines in the separated cell indicate the boundaries of the cell. Many small boundaries in the cell of Fig. 4(b) arise due to unclear scanned parts of the cell that, however, should not be considered as cell defects. The procedure can be briefly summarized as follows:

- a. Cell disjointing and separation;
- b. Cell modification and smoothing;
- c. Fabrication of the NURBS surface using the modified and smoothed cell;
- d. Boolean operation between the surface and a geometric solid cube.

Based on the modeling procedure, over 120 cells were disjointed carefully from the reconstructed model, and all the separated cells were modified and smoothed one by one to fabricate their NURBS surfaces. Fig. 5(a) and (b) display the modified and smoothed outer cells and inner voids, respectively. For simplicity of modeling, all inner voids having small diameters (less than 0.4 mm) were disregarded. This is justified by the fact that the overall stress–strain curve of the specimen is mostly governed by the collapse behavior of large cells because they collapse earlier than small cells. Then, the NURBS surfaces were fabricated using each cell. Fig. 6(a) and (b) show the fabricated surfaces of the outer cells and the inner voids, respectively. A geometric solid of the foam specimen was constructed using Boolean operations between the outer and inner NURBS surfaces and a 10 mm × 10 mm × 10 mm geometric solid cube. The completed geometric solid model for the closed-cell foam specimen is shown in Fig. 6(c).

Subsequently, compatible 3D solid meshes were generated directly in the constructed geometric solid model after numerous iterative calculations using the commercially available mesh generation program PATRAN of MSC Software Corp. (see Fig. 6(d)). In this process, the volume error,  $\frac{V_m - V_a}{V_a}$ , where  $V_m$  is the volume of the meshed model and  $V_a$  is the actual volume of the specimen, was 20.86%. This volume error appears to be quite large for this research. However, a great deal of efforts is required to obtain such magnitude of volume error during the whole modeling process for the actual foam specimen, because the accurate modeling for the thin cell walls is extremely complex and the many small inner voids have to be disregarded for mesh quality assurance. Though we use the meshed model with such volume error, it is regarded that the model may be used for the qualitative analysis of the compressive behavior of the foam specimen.

The Al foam specimen between two loading platens was, therefore, completely modeled by using the finite element model of Fig. 6(d) (see Fig. 7(a) and (b)). Quadratic tetrahedral elements with 10 nodes were used for the specimen and platens. The total number of elements and nodes used were 85,600 and 166,302, respectively. For simulating the compression test process, the FE package code ABAQUS of Dassault Systems was employed. To prevent rigid body motion, the  $x$ - and  $y$ -direction degrees of freedom of several nodes around the center on the lower surface of the specimen were constrained. Moreover, the  $z$ -direction displacement was loaded up to a strain of 5.31% on the top surface of the upper platen, because the plateau stress of the specimen appears in the stress–strain curve before strain reaches 5.31%. Frictionless contact was applied to the contact surfaces between the specimen and the platens, which represents the lubricated surface condition of the platens.

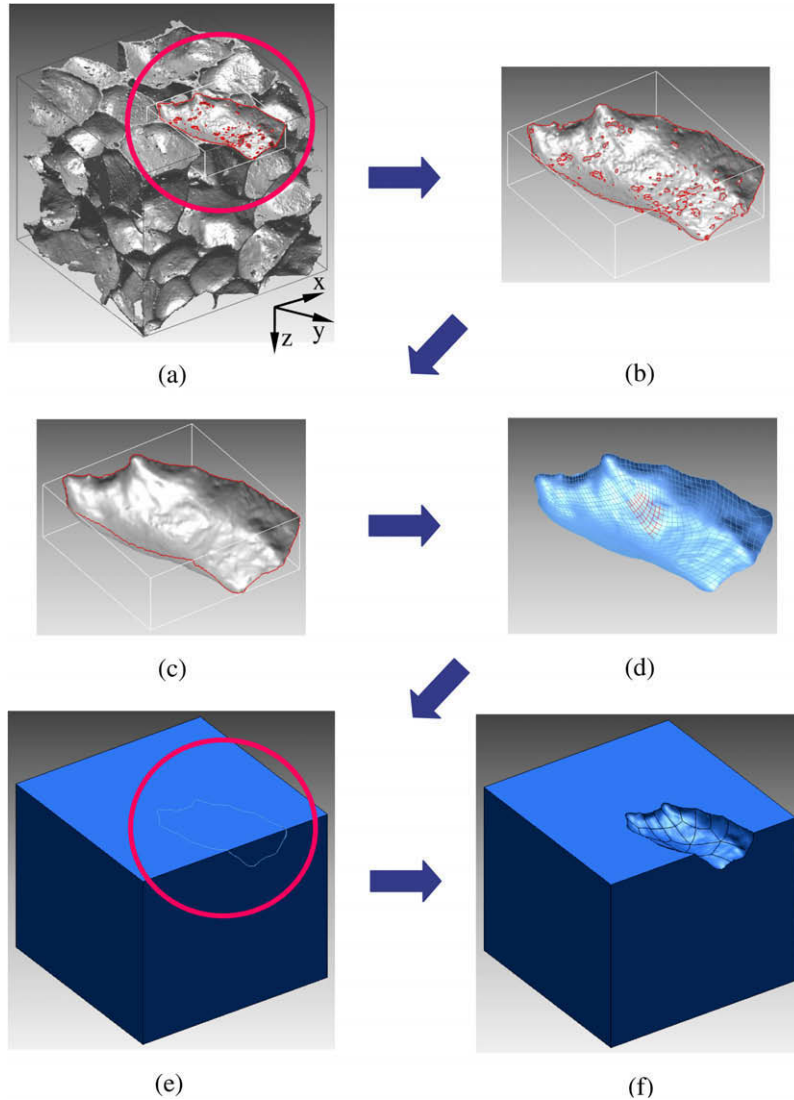


**Fig. 4.** (a) A disjunct cell from the reconstructed model, (b) the separated cell, (c) the modified and smoothed cell, (d) the geometric surface of the cell, (e) the surface with a geometric solid cube and (f) a solid cube after a Boolean operation.

The incremental plasticity theory of isotropic-hardening materials, which uses the objective stress rate for finite deformation, was selected to characterize the elastic–plastic behavior of the Al foam specimen. The constitutive law (McMeeking, 1977; Jeon and Im, 2001; Lee et al., 2007) is given by:

$$\dot{\tau}_{ij} = \frac{E}{1+\nu} \left[ D_{ij} + \frac{\nu}{1-2\nu} D_{kk} \delta_{ij} - \frac{3\sigma'_{ij}\sigma'_{kl}D_{kl} \left( \frac{E}{1+\nu} \right)}{2\sigma^2 \left( \frac{2}{3}h + \frac{E}{1+\nu} \right)} \right] \quad (1.a)$$

for plastic loading and

$$\dot{\tau}_{ij} = \frac{E}{1+\nu} \left[ D_{ij} + \frac{\nu}{1-2\nu} D_{kk} \delta_{ij} \right] \quad (1.b)$$

for elastic loading, where  $E$  is the Young's modulus and  $\nu$  is the Poisson ratio;  $D$  is the rate of deformation tensor defined as the symmetric part of the spatial velocity gradient;

$\delta_{ij}$  is the Kronecker delta; and  $\tau$  is the Kirchhoff stress defined by

$$\tau = \hat{J} \sigma \quad (1.c)$$

Here,  $\hat{J}$  is the ratio of volume in the current state to volume in the reference state and  $\sigma$  is the true stress tensor. Furthermore, let the stress deviator  $\sigma'_{ij}$  and the tensile equivalent stress (Mises stress)  $\bar{\sigma}$  be defined as

$$\sigma'_{ij} = \sigma_{ij} - \frac{1}{3} \delta_{ij} \sigma_{kk}, \quad \bar{\sigma}^2 = \frac{3}{2} \sigma'_{ij} \sigma'_{ij} \quad (1.d, e)$$

Note that the superscript ‘.’ denotes the Jaumann or the corotational stress rate and  $h$  is the slope of the uniaxial Kirchhoff stress versus logarithmic plastic strain curve, which is calculated from the power-law hardening rule of the cell wall material as:

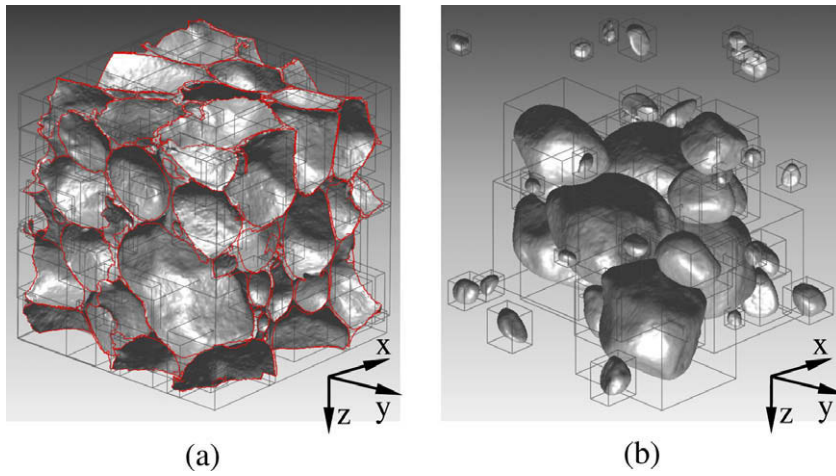


Fig. 5. The modified and smoothed (a) outer cells and (b) inner voids.

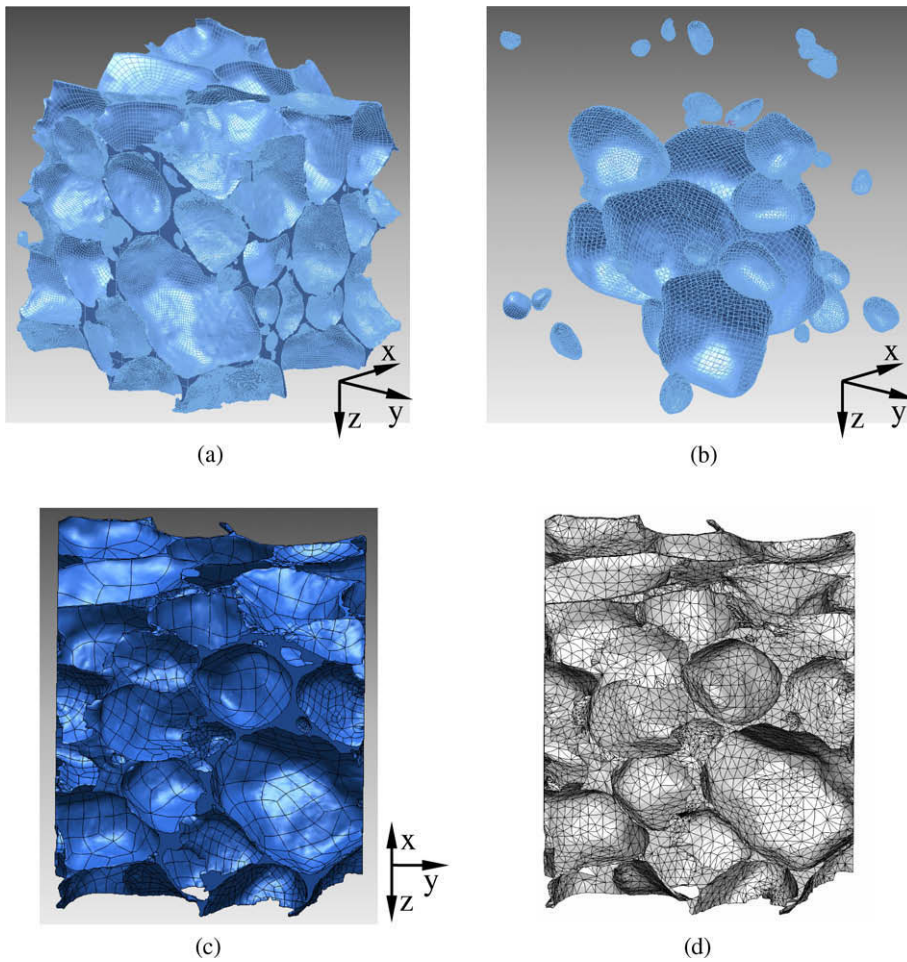


Fig. 6. (a) The NURBS surfaces of the outer cells and (b) the inner voids, and (c) the geometric solid and (d) 3D finite element meshes of the specimen.

$$\frac{\bar{\varepsilon}^p}{\varepsilon_Y} = \alpha \left( \frac{\bar{\sigma}}{\sigma_Y} \right)^m \quad \text{for } \bar{\sigma} > \sigma_Y \quad (2)$$

where  $\sigma_Y$  is the 0.2% offset yield stress;  $\bar{\varepsilon}^p$  is the equivalent plastic strain;  $\varepsilon_Y = \sigma_Y/E$  is the reference strain;  $\alpha$  is a

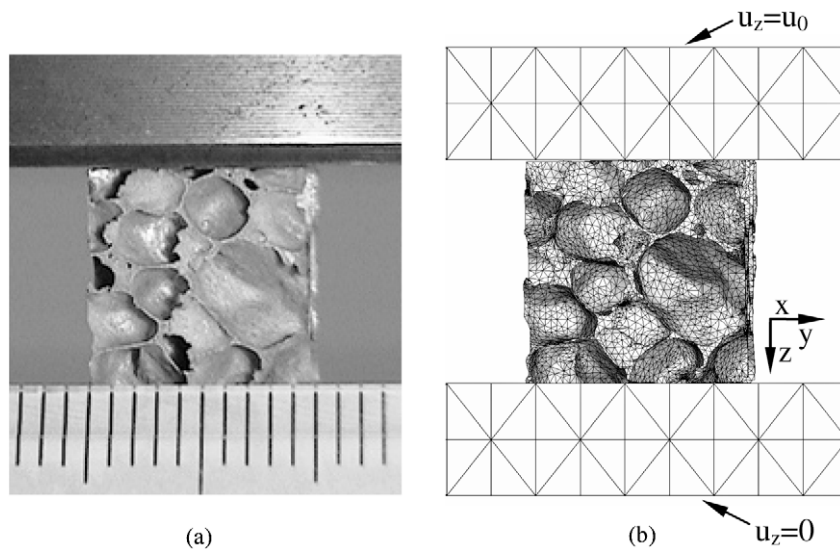


Fig. 7. (a) The Al foam specimen between two loading platens and (b) its finite element modeling.

non-dimensional constant; and  $m$  is the power-law hardening exponent.

Tool steel SKS3 with  $E = 214$  GPa and  $\nu = 0.3$  was used for the loading platens. For the Al cell wall,  $E = 68$  GPa,  $\nu = 0.33$ ,  $\sigma_Y = 35.5$  MPa and  $m = 8.5$  were selected. In particular, the selected value of  $\sigma_Y$  is considerably smaller than the published values,  $\sigma_Y = 120\text{--}170$  MPa (Sugimura et al., 1997; Simone and Gibson, 1998; Andrews et al., 1999). These published values were obtained with an approximation method, which assumes that the yield stress is one-third of cell wall hardness. For the present research, however, we have precisely determined the material properties of the Al cell wall by comparing the force-displacement curves computed using finite element models of two actual  $5\text{ mm} \times 5\text{ mm} \times 5\text{ mm}$  Al foam specimens with the experimentally measured ones (Jeon et al., 2009).

### 3. Uniaxial compression test

The universal testing machine AG-I of SHIMADZU Corp. was used for the uniaxial compression test of the  $10\text{ mm} \times 10\text{ mm} \times 10\text{ mm}$  Al foam specimen, and the designed software for AG-I, TRAPEZIUM, was employed to record the displacement and loading results. A 5 kN load cell was utilized for the test, and the specimen was compressed between two identical circular steel compression platens of diameter 100 mm (see Fig. 7(a)). The platen is sufficiently larger than the specimen, and the parallelism between the two platens was carefully adjusted by examining the contact surface before the compression test. The surfaces of the platens were lubricated to reduce the friction effect of the contact surfaces between the foam specimens and the platens (ASTM E 9-89A, 2000).

Displacement loading was applied to the top surface of the specimen, with a fixed rate of 1 mm/min. The specimen was loaded up to the axial nominal strain of 70% to obtain its entire compressive behavior. The unloading process was begun at 6% of the strain soon after the plastic collapse

stress for measuring the elastic modulus (see Fig. 1). Then the reloading process was continued up to the final strain. The machine compliance, which represents the relation between the displacement of the testing machine and the applied loading, was accounted for to ensure accurate specimen displacements (Jeon and Asahina, 2005).

### 4. Results and discussion

The numerically predicted compressive stress versus nominal strain curve is plotted along with the experimentally measured curve in Fig. 8(a). The computed curve shows qualitative resemblance to the measured one. However, the shape of the plateau stage of the computed curve is somewhat different from that of the measured one, which may be attributed to the relative large volume error (20.86%) of the finite element model used in the computation.

To analyze the detailed plastic collapse mechanisms of the closed-cell Al foam, the compressive stress rate,  $\Delta\sigma/\Delta t$ , and the total equivalent plastic strain rate within the specimen,  $\Delta\varepsilon_{eq}^t/\Delta t$ , were calculated using both the computation and experiment results. Here,  $\Delta t$  was taken from the actual time during the compression test. The stress increments  $\Delta\sigma$  are determined from the load increments (both in testing and computation) divided by the apparent cross sectional area of the specimen. The total equivalent plastic strain increments  $\Delta\varepsilon_{eq}^t$  are determined from computation by taking average over the entire specimen domain. Note that these equivalent plastic strain increments are hardly tractable during compression test due to the extremely inhomogeneous deformation within the specimen.

The calculated  $\Delta\sigma/\Delta t$  was used to determine the initiation of plastic strain zone (or the formation of plastic strain localized band) in the specimen, because the decrease of  $\Delta\sigma/\Delta t$  implies the decreased elastic resistance of the specimen to compressive loading. The calculated  $\Delta\varepsilon_{eq}^t/\Delta t$  was used to determine the initiation of plastic collapse in the specimen because the decrease of  $\Delta\varepsilon_{eq}^t/\Delta t$  means that

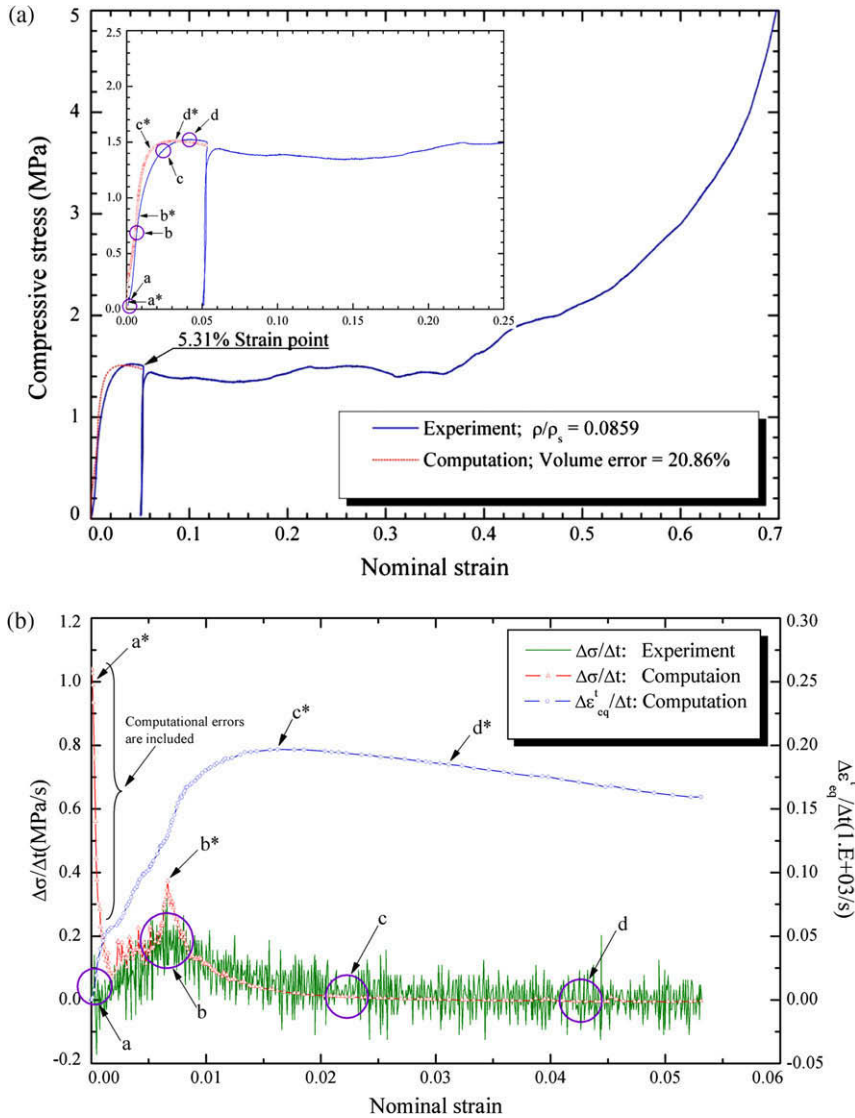


**Fig. 8.** (a) The compressive stress versus nominal strain curve obtained from the experiment and the computation, and (b)  $\Delta\epsilon_{eq}^t/\Delta t$  and  $\Delta\sigma/\Delta t$  obtained from the computational results and the experimental ones.

plastic hinges have formed in the specimen. The calculated  $\Delta\sigma/\Delta t$  and  $\Delta\epsilon_{eq}^t/\Delta t$  values were plotted as functions of applied strain in Fig. 8(b). For comparison,  $\Delta\sigma/\Delta t$  calculated using the experimental results is also plotted. In Fig. 8(a) and (b), the points marked by letters with superscript “\*” represent computational results, while those marked by letters without superscript represent experimental results. Although the experimentally obtained  $\Delta\sigma/\Delta t$  versus nominal strain curve in Fig. 8(b) exhibits severe variations, its overall trend agrees well with that obtained from computation. Therefore, we can investigate changes in deformation state of the specimen using these curves.

The point marked by symbol “a\*” and those in the circled region denoted by “a” in Fig. 8(a) and (b) correspond to the first decrease of  $\Delta\sigma/\Delta t$  under compression. At these points, nonzero total equivalent plastic strain starts to appear in the specimen, and hence “a\*” and “a” represent the

elastic deformation limit of the specimen. Note that the initial high peak of the computed  $\Delta\sigma/\Delta t$  in Fig. 8(b) is mainly caused by computational errors introduced as a result of inaccurate mesh modeling of the actual contact surfaces of the specimen: the computational model assumes a perfectly flat contact surface and complete alignment with the platens, which is hardly achievable in experiments.

Fig. 9(a) displays the deformed configuration of the foam specimen at point “a\*” in Fig. 8(a) and (b). No equivalent plastic strain fields are detected at this early stage, because equivalent plastic strains less than 0.2% are regarded as elastic strains in the present study so that the actual plastic strains in the specimen can be clearly visualized. Beyond point “a\*”, plastic strain fields begin to initiate at the contact surfaces of the specimen with the platens due to nonuniform initial contact. With further increase of loading, these extend to the cell wall (or

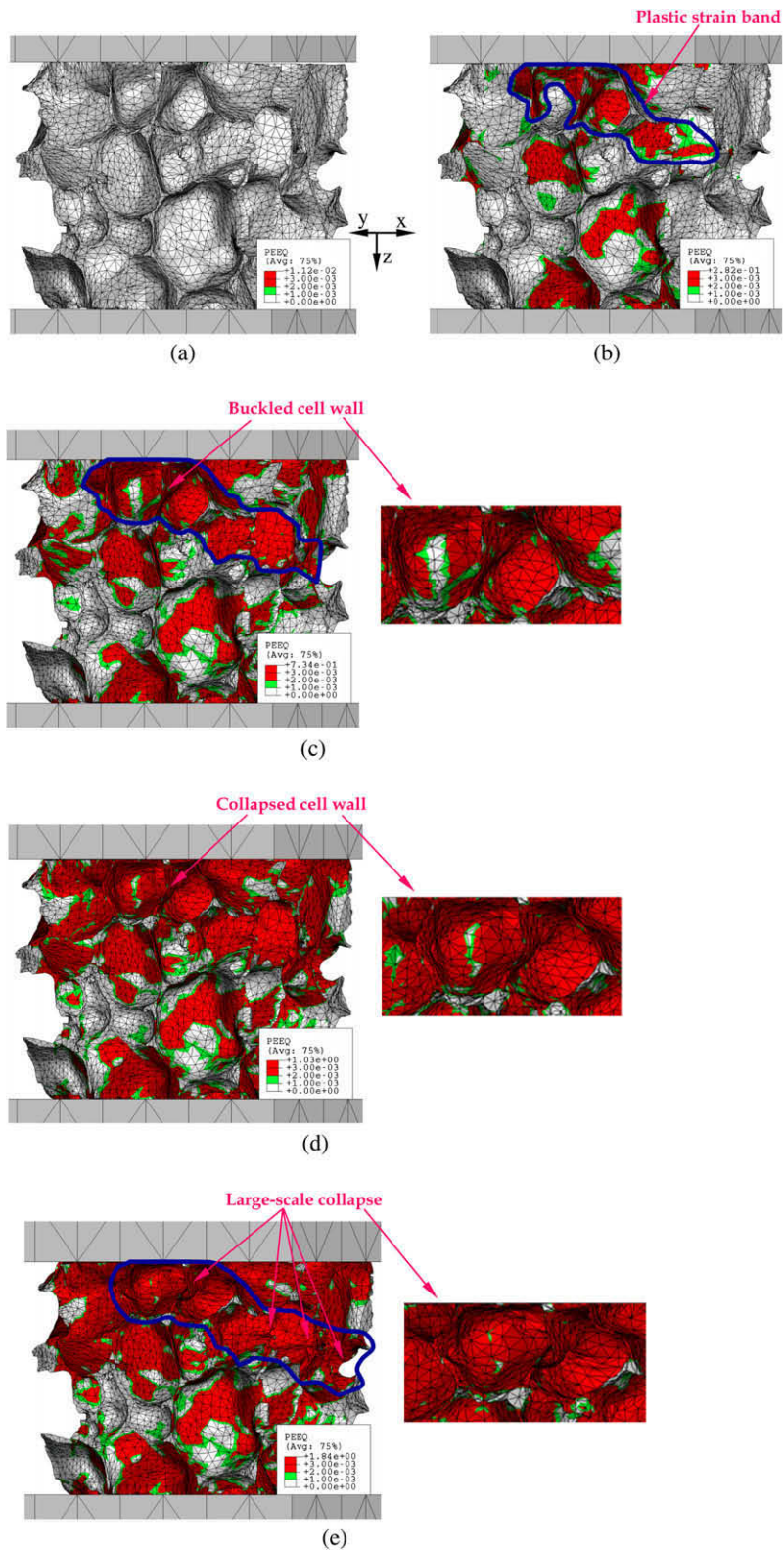


**Fig. 9.** The computed deformation shape of the specimen with its equivalent plastic strain field (a) at position a\*, (b) b\*, (c) c\*, (d) d\* in Fig. 8(a) and (b), and (e) under 5.31% strain. Here, the values in the legends mean the % equivalent plastic strain.

concentrate around defects in the cell wall), as demonstrated below.

Points “b\*” and “b” in Fig. 8(a) and (b) signify the rapid decrease of  $\Delta\sigma/\Delta t$  again after increasing initially beyond points “a\*” and “a”. This indicates a rapid decrease in elastic resistance of the specimen to compressive loading. In fact, these points are associated with the formation of plastic strain localized bands in the specimen. Fig. 9(b) displays the morphology of the deformed specimen at point “b\*”, with locally distributed equivalent plastic strains (greater than 0.2%) marked in red color. The plastic strain band of concern is found within the closed curve (in blue color) shown in Fig. 9(b). With further increase of loading, some of the cell walls within the plastic strain band start to bend and then plastically buckle, as shown in Fig. 9(c).

Points “c\*” and “c” in Fig. 8(a) and (b) are related to the peak value of  $\Delta\varepsilon_{eq}^t/\Delta t$ . While this is evident for “c\*” as it corresponds to the peak value of  $\Delta\varepsilon_{eq}^t/\Delta t$  calculated from computational results, point “c” is not directly decided because  $\Delta\varepsilon_{eq}^t/\Delta t$  can not be calculated using experimentally measured results. Therefore, “c” is estimated indirectly from point “d”, at which the plateau stress is experimentally measured. This is achieved as follows: point “d\*” of Fig. 8(b) corresponds to the point of calculated plateau stress in Fig. 8(a). Assuming that points “c” and “d” have the same stress ratio as that of points “c\*” and “d\*”, we can obtain the stress at “c”, which corresponds to the peak value of the calculated  $\Delta\varepsilon_{eq}^t/\Delta t$ . Fig. 9(c) shows the buckled cell wall and the enlarged plastic strain band relative to that of Fig. 9(b) at point “c\*”.

Beyond points “c\*” and “c”, the value of  $\Delta\varepsilon_{eq}^t/\Delta t$  decreases (Fig. 8(b)) and the plastic strain bands in the cell walls begin to function as plastic hinges. Note that some of the cell walls begin to collapse due to the hinges, which is an interesting result and can also be obtained from the calculation of  $\Delta\varepsilon_{eq}^t/\Delta t$ . This is different from the finding of Bastawros et al. (2000) that the cells do not collapse at this stage.

At points “d\*” and “d” in Fig. 8(a) and (b), the plateau stress is observed. Here, the plastic strain band extends

to fully-developed plastic zones, and large-scale collapse of cell walls begins to occur. Fig. 9(d) displays the collapsed cell wall and the fully-developed plastic zone in the foam specimen. Finally, the completely collapsed foam specimen at the strain of 5.31% is shown in Fig. 9(e) from which the large-scale collapse of cell walls can be observed.

From the present computational results, we vividly showed the existence of plastic strain band in the foam specimen, the typical configuration of the plastic collapse of cell walls, and the precise points on stress versus strain curve for their occurrence, which may not be obtained from experimental investigations. Furthermore, we found that the cause of the plateau stress is not the initial plastic collapse of the foam material, as proposed by Bastawros et al. (2000) based on experimental measurement, but the initiation of large-scale plastic collapse of cell walls.

The detailed mechanisms of cell wall plastic collapse as revealed in Fig. 9 demonstrate that the plastic properties of cell wall material (e.g., 0.2% offset yield stress  $\sigma_Y$  and power-law hardening exponent  $m$ ) significantly influence the compressive behavior of the foam material. In order to investigate the effects of these plastic properties on the energy absorption capacity of the foam material, five numerical case studies were carried out using different values of  $\sigma_Y$  and  $m$  of the cell wall material. In two case studies, the same value of  $m = 8.5$  but two different values of  $\sigma_Y$  (45 MPa and 55 MPa) were used. In another two case studies,  $\sigma_Y$  was fixed at 35.5 MPa while two different  $m$  (7 and 5.5) were chosen. For the last case study,  $\sigma_Y = 55$  MPa and  $m = 5.5$  were selected.

Fig. 10 shows the uniaxial compressive stress–strain curves computed from the above five case studies. It is seen from Fig. 10 that an increase in the 0.2% offset yield stress considerably increases the magnitude of the plateau stress, while a decrease in the power-law hardening exponent not only increases the magnitude of the plateau stress but also changes the initial shape of the plateau stage. Also, it is found that the magnitude of the plateau stress is dramatically increased if the 0.2% offset yield stress is increased

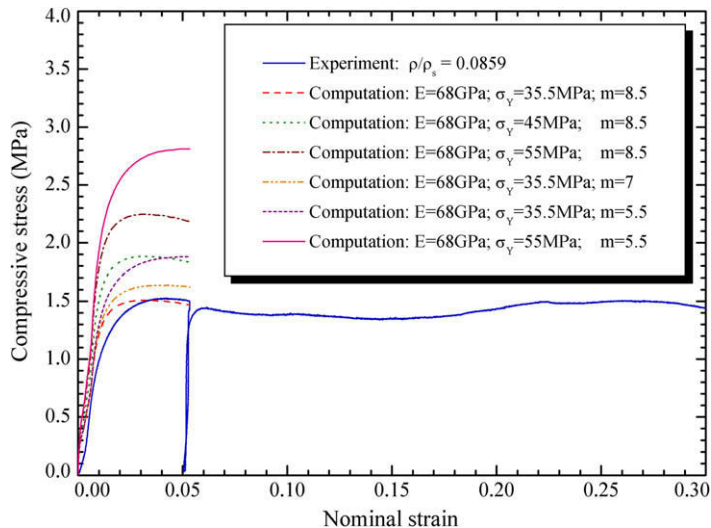


Fig. 10. Compressive stress versus nominal strain curves computed using different values of  $\sigma_Y$  and  $m$ .

and the power-law hardening exponent is decreased simultaneously (see the stress–strain curve of the last case study in Fig. 10). Therefore, in order to improve the energy absorption capacity of the metallic foam, effective techniques for increasing the 0.2% offset yield stress of the cell wall material accompanied with decreasing its power-law hardening exponent are required. For example, with the direct foaming method, this may be achieved by adding suitable metal components to the raw material of the cell wall (see, e.g., Zhang et al., 2009).

## 5. Conclusions

The detailed deformation and plastic collapse mechanisms of closed-cell Al foams under uniaxial compression are analyzed using both the methods of finite elements and experimental measurements. A three-dimensional finite element model for a real closed-cell Al foam specimen was constructed by employing the microfocus X-ray CT system, the 3D reconstruction program, the 3D scanned data processing software, and the commercially available mesh generation program. Finite element analysis is subsequently carried out using the constructed finite element model.

The compressive stress rate,  $\Delta\sigma/\Delta t$ , and the total equivalent plastic strain rate within the specimen,  $\Delta\epsilon_{eq}^c/\Delta t$ , were introduced to investigate the change in deformation state of the specimen. The results show that the formation of plastic strain localized bands in the cell walls causes the plastic collapse of the foam material, and that cell wall collapse is initiated by plastic hinges formed in the plastic strain bands. Furthermore, it is demonstrated that large-scale plastic collapse of cell walls and not their initial plastic collapse occurs as the plateau stress is reached.

The effects of the plastic properties of cell wall material on the compressive behavior of the foam material were quantified. It is found that an increase in the 0.2% offset yield stress considerably increases the magnitude of the plateau stress, whereas a decrease in the power-law hardening exponent not only increases the magnitude of the plateau stress but also modifies the shape of the plateau stage. Moreover, it is found that an increase in the 0.2% offset yield stress with a decrease in the power-law hardening exponent dramatically increases the magnitude of the plateau stress. Therefore, controlling the plastic properties of the cell wall material by adding suitable metal components should be an effective and efficient method to improve the energy absorption capacity of the foam material.

## Acknowledgement

I. Jeon would like to thank Dr. Yasuo Yamada, Dr. Tsutomu Sonoda and Mr. Kiyotaka Katou of AIST for discus-

sions about the experimental process and technical supports. This study was supported by National Research Lab program of the Korea Science & Engineering Foundation (ROA-2006-000-10249-0).

## References

- Andrews, E., Sanders, W., Gibson, L.J., 1999. Compressive and tensile behaviour of aluminum foams. *Mater. Sci. Eng. A* 270, 113–124.
- Banhart, J., 2001. Manufacture, characterization and application of cellular metals and metal foams. *Prog. Mater. Sci.* 46, 559–632.
- Bastawros, A.F., Bart-Smith, H., Evans, A.G., 2000. Experimental analysis of deformation mechanisms in a closed-cell aluminum alloy foam. *J. Mech. Phys. Solids* 48, 301–322.
- Brydon, A.D., Bardenhagen, S.G., Miller, E.A., Seidler, G.T., 2005. Simulation of the densification of real open-celled foam microstructures. *J. Mech. Phys. Solids* 53, 2638–2660.
- E 9-89A, 2000. Standard Test Methods of Compression Testing of Metallic Materials at Room Temperature. ASTM, Philadelphia.
- Evans, A.G., Hutchinson, J.W., Ashby, M.F., 1999. Multifunctionality of cellular metal systems. *Prog. Mater. Sci.* 43, 171–221.
- Jeon, I., Asahina, T., 2005. The effect of structural defects on the compressive behavior of closed-cell Al foam. *Acta Mater.* 53, 3415–3423.
- Jeon, I., Im, S., 2001. The role of higher order eigenfields in elastic–plastic cracks. *J. Mech. Phys. Solids* 49, 2789–2818.
- Jeon, I., Katou, K., Sonoda, T., Asahina, T., Kang, K.J., 2009. Cell wall mechanical properties of closed-cell Al foam. *Mech. Mater.* 41, 61–73.
- Lee, Y.H., Lee, B.K., Jeon, I., Kang, K.J., 2007. Wire-woven Bulk Kagome (WBK) truss cores. *Acta Mater.* 55, 6084–6094.
- McMeeking, R.M., 1977. Finite deformation analysis of crack-tip opening in elastic–plastic materials and implications for fracture. *J. Mech. Phys. Solids* 25, 357–381.
- Miyoshi, T., Itoh, M., Mukai, T., Kanahashi, H., Kohzu, H., Tanabe, S., Higashi, K., 1999. Enhancement of energy absorption in a closed-cell aluminum by the modification of cellular structures. *Scripta Mater.* 41, 1055–1060.
- Shin, D.S., Lee, K., Kim, D., 2007. Biomechanical study of lumbar spine with dynamic stabilization device using finite element method. *Comput.-Aided Des.* 39, 559–567.
- Simone, A.E., Gibson, L.J., 1998. Aluminum foams produced by liquid-state processes. *Acta Mater.* 46, 3109–3123.
- Sone, T., Tamada, T., Jo, Y., Miyoshi, H., Fukunaga, M., 2004. Analysis of three-dimensional microarchitecture and degree of mineralization in bone metastases from prostate cancer using synchrotron microcomputed tomography. *Bone* 35, 432–438.
- Spanne, P., Thovert, J.F., Jacquin, C.J., Lindquist, W.B., Jones, K.W., Adlar, P.M., 1994. Synchrotron computed microtomography of porous media: topology and transports. *Phys. Rev. Lett.* 73, 2001–2004.
- Sugimura, Y., Meyer, J., He, M.Y., Bart-Smith, H., Grenstedt, J., Evans, A.G., 1997. On the mechanical performance of closed cell Al alloy foams. *Acta Mater.* 45, 5245–5259.
- Toda, H., Ohgaki, T., Uesugi, K., Kobayashi, M., Kuroda, N., Kobayashi, T., Niinomi, M., Akahori, T., Makii, K., Aruga, Y., 2006. Quantitative assessment of microstructure and its effects on compression behavior of aluminum foams via high-resolution synchrotron X-ray tomography. *Metall. Mater. Trans. A* 37, 1211–1219.
- Youssef, S., Marie, E., Gaertner, R., 2005. Finite element modeling of the actual structure of cellular materials determined by X-ray tomography. *Acta Mater.* 53, 719–730.
- Zhang, B., Kim, T., Lu, T.J., 2009. The solidification of two-phase heterogeneous materials: theory versus experiment. *Sci. China E* 52, 1688–1697.